A High-Flux Accelerator-Based Neutron Source for Fusion Technology and Materials Testing[1]

G. P. Lawrence,[2] G. L. Varsamis,[2,3] T. S. Bhatia,[2] B. Blind,[2] F. W. Guy,[2] R. A. Krakowski,[2] G. H. Neuschaefer,[2] N. M. Schnurr,[2] S. O. Schriber,[2] T. P. Wangler,[2] and M. T. Wilson[2]

Advances in high-current linear-accelerator technology since the design of the Fusion Materials Irradiation Test (FMIT) Facility have increased the attractiveness of a deuterium-lithium neutron source for fusion materials and technology testing. This paper discusses the conceptual design of such a source that is aimed at meeting the near-term requirements of a high-flux high-energy International Fusion Materials Irradiation Facility (IFMIF). The concept employs multiple accelerator modules providing deuteron beams to two liquid-lithium jet targets oriented at right angles. This beam/target geometry provides much larger test volumes than can be attained with a single beam and target and produces significant regions of low neutron-flux gradient. A preliminary beam-dynamics design has been obtained for a 250-mA reference accelerator module. Neutron-flux levels and irradiation volumes were calculated for a neutron source incorporating two such modules, and interaction of the beam with the lithium jet was studied using a thermal-hydraulic computer simulation. Approximate cost estimates are provided for a range of beam currents and a possible facility staging sequence is suggested.

KEY WORDS: particle accelerator; high-flux neutron source; deuterium-lithium reactions; fusion materials testing.

1. INTRODUCTION AND BACKGROUND

According to a recent international assessment of fusion technology and materials-testing needs,[1] the present understanding of materials behavior in a

fusion-reactor radiation environment is insufficient to guarantee the required performance and endurance of future fusion-reactor components. The perceived need for a high-flux materials-testing neutron source to address this problem resulted in an International-Energy-Agency (IEA) initiative to examine neutron source requirements and to evaluate the technologies available for meeting them in the near term. The IEA initiative fostered a series of regional meetings (in the U.S., Europe, and Japan) throughout 1988 to consider neutron-source options and requirements, and culminated in February 1989 with an international workshop[2] in San Diego to select the most promising source candidates.

This paper describes an accelerator-driven neutron-source concept that has been developed during the past year,[3-5] and that was presented at the San Diego workshop. The scheme is based on the same general approach as that proposed in the Fusion Materials Irradiation Test (FMIT) facility,[6] but takes advantage of improvements in the technology of high-current ion accelerators[7,8] that have occurred during the past decade to offer a more attractive and cost-effective facility for fusion materials testing. As in FMIT, 35-MeV deuterons are used to generate a fusion-like neutron spectrum from the thick-target neutron yield of the $Li(d,n)$ nuclear stripping reaction.[9] This spectrum, which peaks near a neutron energy of 14 MeV, produces atomic displacements (dpa) and transmutation products, e.g., Helium, in irradiated materials with ratios that bracket the complete range of expected fusion reactor environments. Also, because the deuteron energy is adjustable, the dpa/He ratio can be tuned to evaluate possible spectrum-dependent effects.

The FMIT concept involved a single (100-mA) beam incident on a single lithium target. The useful test volume was relatively modest and steep neutron-flux gradients were a significant concern for materials experimenters. The improved D-Lithium scheme presented here proposes two deuteron beams incident on two lithium targets at right angles, arranged in the configuration shown in Fig. 1. The beams would be generated by accelerator modules
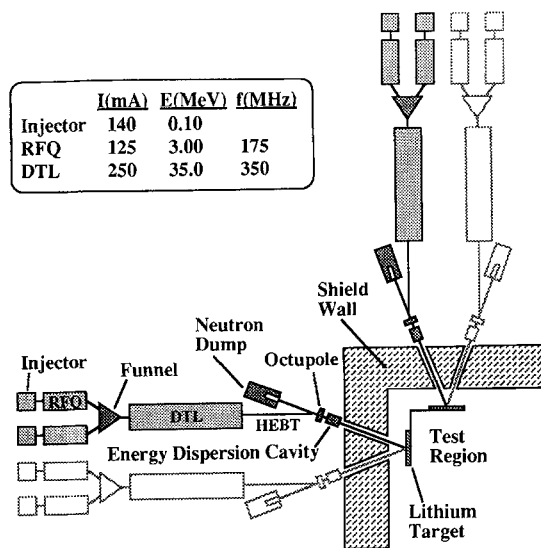
capable of delivering up to 250 mA each. With a total delivered current of 500 mA and an orthogonal target geometry, much greater materials-test volumes can be obtained than in FMIT, at equivalent neutron wall-loading-power levels relevant to expected fusion-reactor environments. The two-target geometry and modular accelerator system provides considerable flexibility in the achievable neutron-flux levels and test volumes, and also permits flux-gradient tailoring, staged expansion of testing capability, and improved facility availability.

This paper focuses on a reference design consisting of a two-module neutron source, with each deuteron accelerator delivering a 250-mA cw beam. Each module would consist of two D^+ dc injectors, two radio-frequency quadrupoles (RFQs), a beam funnel, and a single drift-tube linac (DTL). The reference neutron source contains two lithium jet targets oriented at 90° with respect to each other, with each target receiving one beam. However, even within the framework of a two-beam, two-target system, many other design variations are certainly possible. As implied in the figure, the total deuteron current could be expanded to 1000 mA in a straightforward way by adding two more accelerator modules, or it could be reduced to 250 mA (or less) by eliminating one RFQ from each module.

The paper presents a conceptual design for a 250-mA accelerator module, assesses the capability of a lithium jet target to handle the deuteron beam power, describes the neutron environment for materials testing generated by a two-module D-Lithium source, and addresses the suitability of the neutron spectrum for fusion-relevant measurements. It describes a possible facility-staging sequence, and summarizes construction and operating costs for a range of facility scales. Finally, a figure-of-merit relationship is derived, to allow comparison between the D-Lithium neutron source concept and other proposed fusion-technology neutron sources.

1.1. FMIT Technology Base

The FMIT facility, designed in 1978–1981, was to provide a 100-mA deuteron beam to a lithium-jet target, generating a 0.5-liter test volume exposed to a minimum uncollided neutron flux of 10^{14} n/cm²/s (equivalent to a fusion-reactor wall-loading power of about 2.3 MW/m²), and a 10-cm³ volume at 10^{15} n/cm²/s (about 23 MW/m²). Flux gradients in the test zone were relatively steep. The accelerator con-

	I(mA)	E(MeV)	f(MHz)
Injector	140	0.10	
RFQ	125	3.00	175
DTL	250	35.0	350

Fig. 1. Reference neutron source: Two 250-mA accelerator modules and two lithium targets. Lightly-drawn modules indicate upgrade potential.

sisted of a 100-keV D^+ cw injector followed by a 2-MeV RFQ and a 35-MeV DTL, both operating at a frequency of 80 MHz. The DTL accelerating gradient was 1 MV/m, and the total rf power required was 5.4 MW. The deuteron beam was to be conveyed to the lithium jet by a high-energy beam-transport (HEBT) system that included an energy-modulating rf cavity for broadening the beam energy spread to 0.5 MeV (rms). Lithium flow rate in the jet was 17.3 m/s, and peak beam-power deposition density in the jet reached 1.8 MW/cm³.

Before the project was terminated in 1984, FMIT firmly established the general technical feasibility of the D-Lithium source concept at the listed parameter values. The main accomplishments of the program included neutronics calculations to determine test-cell flux levels and volumes, thermal-hydraulic calculations to model the beam/target interaction, development and operation of a prototype lithium jet and circulation system, construction and cw operation of a prototype injector and RFQ, and a complete engineering design for the facility.

2. NEW ACCELERATOR CONCEPT
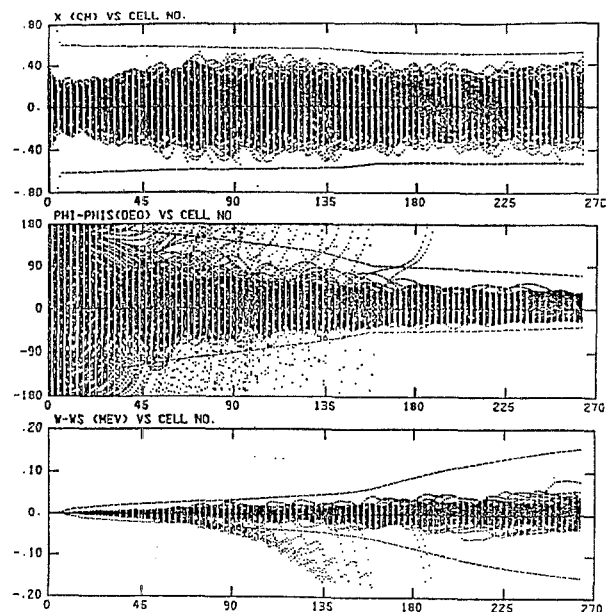
Since the completion of the FMIT design, there

Fig. 2. Beam parameters in RFQ vs. PARMTEQ cell number: horizontal displacement (cm) (top), phase deviation from synchronous (degrees) (middle), and energy deviation from synchronous (MeV) (bottom).

have been significant advances in high-current ion-linac technology that will allow construction of an improved D-Lithium neutron source, with higher performance at significantly lower cost per neutron. These advances include a comprehensive emittance-growth theory, better beam-dynamics simulation codes, development of the beam-funneling concept for current multiplication through rf frequency doubling, the use of high accelerating-structure frequencies plus permanent-magnet quadrupoles (PMQ) plus ramped accelerating gradients to control beam-emittance growth and halo growth, and the use of high-order optics in beam-transport systems to manipulate beam profiles.

The 250-mA accelerator module suggested as the building block of the reference source concept is sketched in Fig. 1, which also tabulates the frequencies, currents, and energies selected for each component. Preliminary beam dynamics simulations have been carried out for this module and are discussed in the following section.

2.1. Injector, RFQ, and Funnel

Because of beam loss inherent in the bunching process of the RFQ, about 140 mA of D^+ must be provided by the injector (at an energy of 100 keV) to obtain 125 mA at the RFQ output. This requirement could be met by a duopigatron ion source similar to one operating at Chalk River Nuclear Laboratory.[10] The selected RFQ frequency (175 MHz) is more than twice that of FMIT, allowing a large reduction in transverse structure dimensions. High-power (0.5–1.0 MW cw) tetrodes are commercially available to provide rf power for acceleration.

Beam behavior in the RFQ was simulated with the code PARMTEQ, using a 1000-super-particle input distribution that uniformly filled a four-dimensional transverse phase-space hyperellipsoid. The longitudinal input distribution was that of a continuous beam with zero energy spread. Figure 2 shows the radial distribution, phase width, and energy spread of these particles as the beam traverses the RFQ. Table I lists important RFQ parameters not displayed in Fig. 1; the transverse (T) and longitudinal (L) beam emittances shown are normalized rms values.

The output beams from the two RFQs are combined longitudinally at twice the RFQ frequency in a funnel of the type soon to be tested at Los Alamos, and depicted schematically in Fig. 3. At the funnel

Table I. RFQ Parameters

Mean aperture	1.2 cm
Tank diameter	36 cm
Structure length	5.4 m
Surface field (peak)	25 MV/m
Transmission	89.3%
rf power (copper)	0.3 MW
rf power (beam)	0.4 MW
rf power (total)	0.7 MW
Output emittance (T)	0.27π mm-mrad
Output emittance (L)	0.46π mm-mrad

entrance, the beams are 16.4 cm apart and are converging at a relative angle of 20°. Each beam is transported separately through four PMQs and a 175-MHz buncher to the beam-combining elements, which consist of a large-aperture defocusing PMQ and a 175-MHz rf-deflection cavity. The bunches from each RFQ are separated by 180° in phase, and are kicked onto a common longitudinal axis by the rf deflector cavity. An additional four PMQs and two 350-MHz bunchers provide a six-dimensional phase-space match from the funnel into the DTL. Beam dynamics calculations for the funnel show that rms-emittance growth is small.

2.2. Drift-Tube Linac

The DTL consists of two 350-MHz tanks operating as $1\beta\lambda$ accelerating structures (β = matched particle speed as fraction of speed of light; λ = rf wavelength). The focusing pattern of the drift-tube quadrupoles is FOFODODO (F = focusing quad, D

= defocusing quad, O = drift space), and their field gradient is ramped from 120 to 100 T/m with increasing beam energy. The accelerating field in the first tank is ramped from 3 to 4 MV/m, while in the second the field is held constant at 4 MV/m. Radiofrequency power would be supplied by 1-MW cw, 350-MHz klystrons that are available from at least two manufacturers. The frequency is more than four times that of FMIT, and the accelerating gradient is three to four times higher, resulting in a much more compact accelerator. Improved control of beam halos (and reduced beam loss) is expected with the higher frequency structure.

The simulation code PARMILA was run with 1000 superparticles to examine the DTL beam dynamics at 250 mA. The input phase-space distribution is that of a uniformly filled six-dimensional hyper-ellipsoid whose rms emittances are obtained from the RFQ and funnel outputs. No particles from this distribution were lost from interception by the drift tubes. Figure 4 shows the beam's radial dimension as it traverses the DTL, along with its phase width and energy spread. Table II lists important DTL parameters not mentioned previously.

2.3. High-Energy Beam Transport

Details of the high-energy beam-transport (HEBT) systems that convey the 35-MeV deuterons to the lithium targets have not been completed. However, the general requirements and features are clear. The HEBT for each module will consist of a periodic focusing transport line of quadrupoles, and will in-
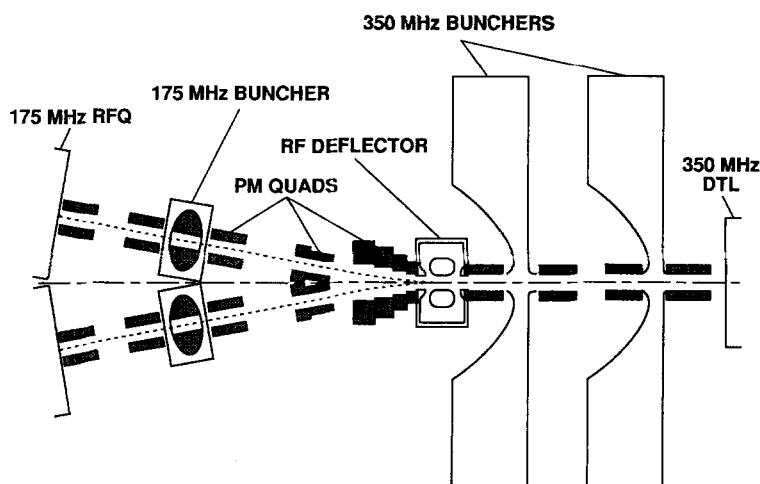

Fig. 3. Schematic of funnel for reference accelerator module.
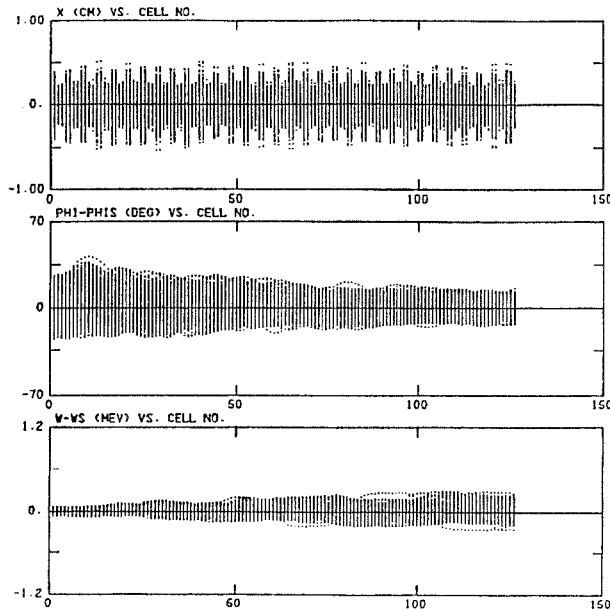
Fig. 4. Beam parameters in DTL vs. PARMILA cell number: horizontal displacement (cm) (top), phase deviation from synchronous (degrees) (middle), and energy deviation from synchronous (MeV) (bottom).

Fig. 5. Beam-energy spread growth in HEBT from space-charge forces.

Table II. DTL Parameters

Tank diameter	50 cm
Number of drift tubes	128
Drift-tube aperture	2.0 cm
Total length	13 m
Beam loading	71%
rf power (copper)	3.3 MW
rf power (beam)	8.0 MW
rf power (total)	11.3 MW
Output emittance (T)	0.30π mm-mrad
Output emittance (L)	0.51π mm-mrad

clude at least one (achromatic) bend so that back-angle neutrons emitted from the target strike a shielded dump rather than the accelerator. A spur beamline and a high-power beam stop will be needed to permit accelerator tuning (at reduced duty factor) before beam is switched to the target. Special elements will be inserted into the HEBT to increase the beam's energy spread to 1.0 MeV (rms) and to flatten and widen the transverse distribution. These manipulations are required to maintain sufficiently low peak power-deposition density in the lithium jet.

Forces both internal and external to the beam can be used to obtain the required deuteron energy spread. If the periodic-focusing system at the end of
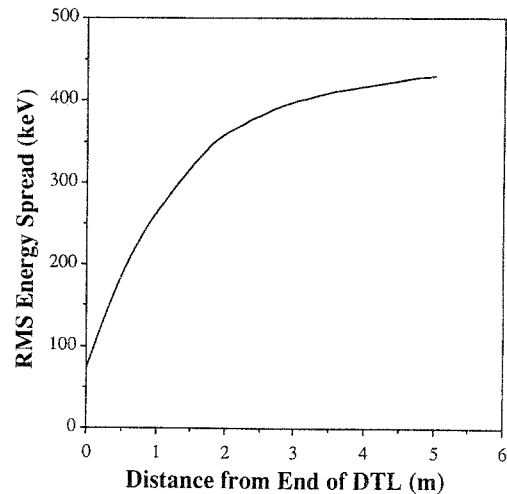
the DTL is continued into the HEBT with the same lattice parameters, the longitudinal space-charge forces within each beam bunch will increase the rms energy spread from 70 keV at the end of the linac to 500 keV within five meters of drift space. The dependence of beam energy spread on distance from the end of the accelerator is shown in Fig. 5 for a 250-mA beam. The required additional 500 keV beam energy spread can be provided by a 2-MV, 350-MHz energy-dispersion cavity placed near the end of the HEBT, at a distance where adequate correlation exists between relative particle energy and relative longitudinal position in the beam bunches.

Calculations made for a separate project suggested the feasibility of using non-linear optics (octupoles) in the HEBT to produce a ribbon beam with a flat density profile[11] in the horizontal plane (normal to the flow direction) at the lithium target. This kind of density profile would provide definite advantages in comparison with the two-dimensional Gaussian beam distribution assumed in the FMIT design. In addition to lowering the peak power deposition in the target, a ribbon beam would generate a more uniform neutron-flux distribution in the test volume. Calculations made with the optics code PATH for a 250-mA beam of 35-MeV deuterons show that it is possible to produce a 4-cm-wide nearly-flat density distribution in the horizontal plane and a 1-cm-rms Gaussian density profile in the orthogonal plane. These profiles, which are displayed in Fig. 6, were achieved using a single 1-m-long octupole located 2.5 m from the lithium target. The octupole strength
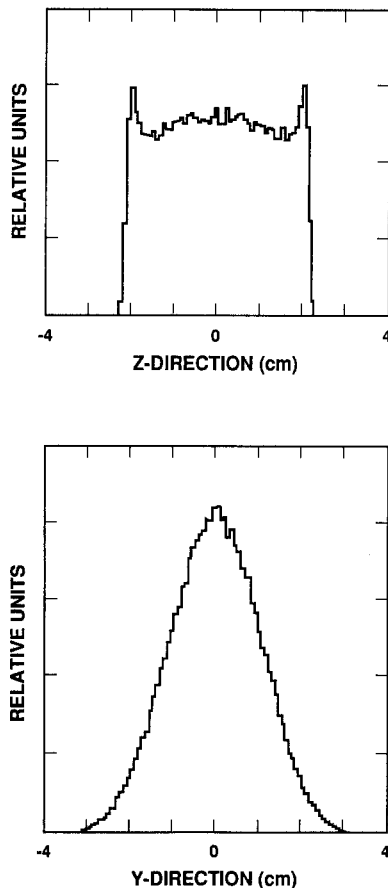
Fig. 6. Beam-density distribution at lithium target produced by 4800 T/m^3 octupole in HEBT; z-direction is perpendicular to flow, y-direction is along flow.

required is 4800 T/m^3, which is a practical value for a magnet having a 10-cm bore. The y and z density distributions in the figure are plotted on the same vertical scale. Apparent fluctuations in the density profile are numerical effects due to the finite number of particles used in the calculation.

3. FACILITY CONCEPT

In addition to higher deuteron currents achieved in a more compact accelerator geometry, the two principal features of the new D-Lithium source concept that offer major improvements over FMIT are: (1) compatibility with a staged design and construction approach, and (2) a two-target, two-beam geometrical configuration. The following section describes a possible facility staging scenario, and then
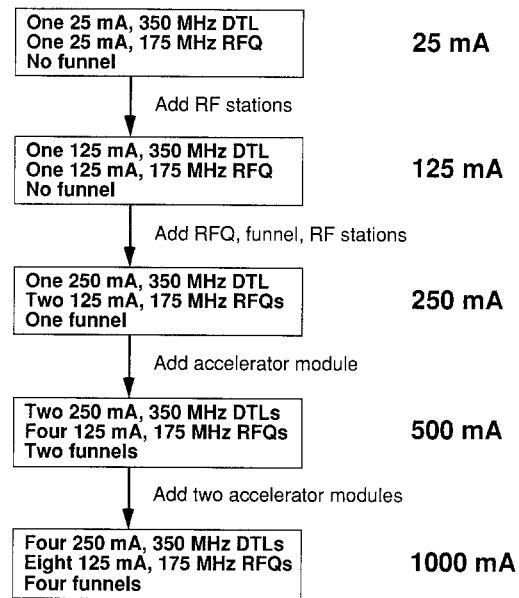

Fig. 7. Schematic of a D-Lithium source staging sequence from a 25-mA to a 1000-mA facility.

briefly describes the envisioned beam/target geometry.

3.1. Staged Design and Construction

As indicated in Section 2, the basic building blocks of the reference accelerator module are a 100-keV dc injector, a 175-MHz RFQ, and a 350-MHz DTL. Figure 7 illustrates a possible facility staging sequence based on this modular framework. The first stage would include a single injector, RFQ, and DTL, and could begin operation with a relatively modest deuteron current, say 25 mA. The RFQ and DTL would be constructed from the beginning with extra rf-feed ports, but the initial complement of rf stations would only be sufficient to accelerate 25 mA. By adding rf stations, the current capability of the accelerator could be raised to 125 mA without any major changes in the general configuration. In the next stage, a second injector and RFQ would be added, a funnel would be installed, and more rf stations added in the DTL to handle the increased beam current. Beam output would be doubled to 250 mA. Up to this point, the most cost-effective overall facility configuration would probably be to split the output beam in the HEBT (by an inverse funneling process) in order to bombard two lithium targets. The next stages involve straightforward multiplica-
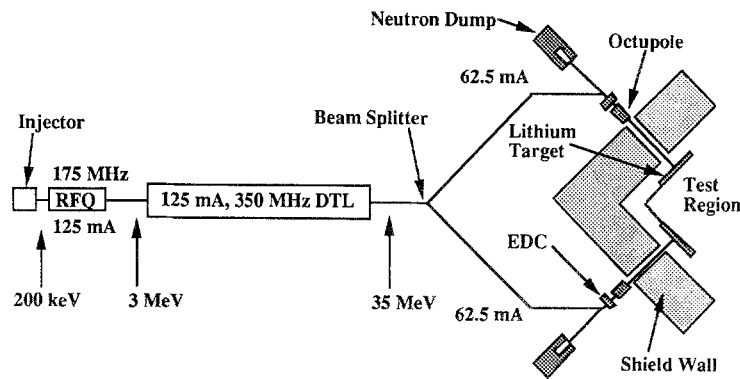
Fig. 8. Layout of D-Lithium source with one 25–125-mA accelerator and beam splitting in HEBT.

tion of the basic 250-mA accelerator module, first by a factor of two (reference system), and finally by a factor of four to reach a maximum of 1000 mA. Beam splitting in the HEBT is not needed for the final stages.

The staged implementation approach permits accelerator and target testing at gradually increasing levels, and overall system evaluation in measured increments. It avoids commitment of the entire capital investment of a large full-scale facility up front. At every completed stage, a materials testing program can be carried out, the fusion materials database expanded, and the desirability of increasing the neutron flux and experimental volume (by upgrading to the next stage) can be determined.

Figures 8 and 9 show the facility configuration for a 25- to 125-mA system and a 250-mA system, respectively. Figure 1 shows the configuration of the 500-mA reference system and also suggests the final upgrade to 1000 mA. These figures also show

(schematically) some important features of the overall machine layout, including neutron dumps for stopping back-angle neutrons streaming from the lithium targets, octupoles in the HEBTs for flattening the target beam-density distribution, and energy-dispersion rf cavities (EDC) for increasing the deuteron-beam energy spread. The latter elements (and the accelerator modules themselves) are shielded from the neutron source by 1-m-thick steel and concrete wall. In the sketch layouts of Figs. 1, 8, and 9, the deuteron beams are shown incident on the targets at an exaggerated angle with respect to the normal. In the real configuration, the beam angles would be about 5°.

3.2. Beam/Target Geometry

A fundamental design characteristic of the reference D-Lithium neutron source is the use of two
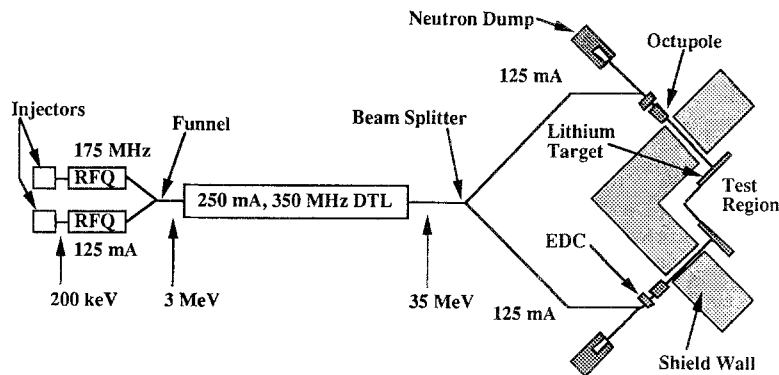

Fig. 9. Layout of D-Lithium source with one 250-mA accelerator and beam splitting in the HEBT.

targets in a facing geometry irradiating the same test volume. This arrangement provides a marked improvement over the FMIT design from several points of view.

The two-target design permits considerable flexibility in the test cell configuration and experimental utilization. Targets may be operated independently or jointly, according to the test requirements. With dual target operation, regions of low- and/or high-flux gradient can be found in the test region at different locations. Thus, experiments can be optimized for low-gradient or high-gradient environments by proper positioning in the test zone. Alternatively, identical material specimens could be exposed simultaneously to low- and high-flux gradients and the resulting damage compared to study gradient effects.

The constant-flux test volume and its volume-to-area aspect ratio could be optimized at specific neutron flux levels by means of small variations in the relative orientation and spacing of the lithium targets. For example, by suitable adjustment of these parameters, experimenters could have nearly-uniform flux over a large-area flat sample, a long rod-shaped sample, or a moderate-sized spherical or box-shaped sample. In general, the two target configuration provides a continuum of trade-offs between test volume, flux level, and gradient that can be tuned to suit experimenter requirements. More details of the potential of the D-Lithium source for test optimization are provided in Sections 4.4 and 4.5.

Figure 10 is an illustration of the target and sample-test region showing two lithium jets oriented at 90° to each other and spaced about 10 cm from their common vertex. The viewing position is outside the shield wall, midway between the deuteron beams, and above the horizontal midplane. Each target may be served by a separate lithium circulation system in order to enhance overall system availability and maintainability. The lithium is pumped upward in the feed tubes, then flows downward at high speed through the target zone, and is received in collection tanks below. A representative materials-test volume measuring about 30 cm × 30 cm × 30 cm is indicated behind the lithium jets.

A close-up view of the beam/target interaction zone is shown in Fig. 11. The lithium flows into a jet-forming nozzle through a flow straightener that is used to eliminate large-scale turbulence. A 1.9-cm thick liquid-lithium jet exits the nozzle and flows along a curved thin steel wall, with its free surface exposed to the incident deuteron beam. The 35-MeV deuterons are completely stopped in the lithium, and since only a small fraction produce neutrons, most of the beam energy is deposited in the jet. The centrifugal force introduced by the curved flow path (concave toward the beam) increases the internal pressure sufficiently in the jet to prevent local boiling at the
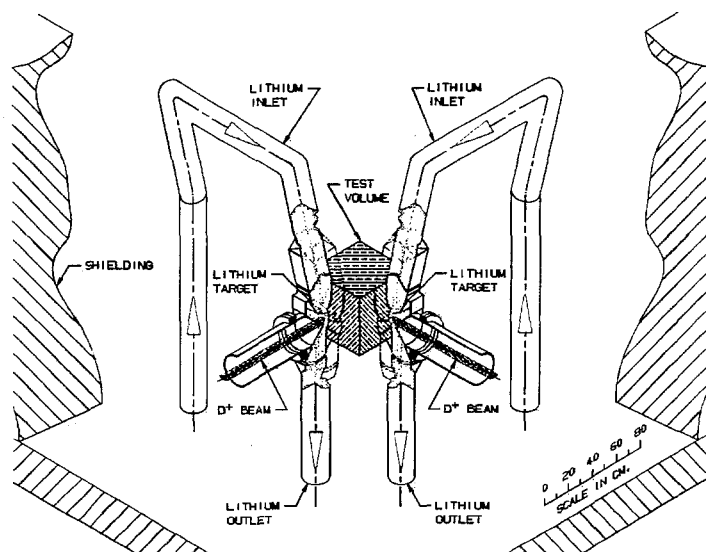

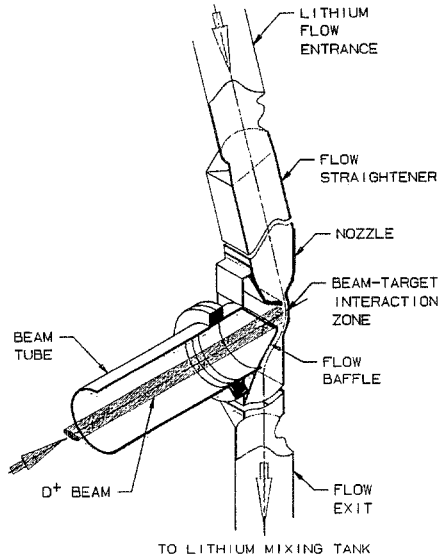Fig. 10. Schematic of the target and test zone.

Fig. 11. Detailed layout of the beam/target interaction zone.

point where the deuteron peak energy deposition occurs.

4. TARGET NEUTRONICS

Analysis of the neutron flux and available test volumes in the experimental region are as important for a complete description of the D-Lithium source as the deuteron beam-delivery system design and lithium jet target design. The following sections discuss the neutron source function generated by the interaction of the deuteron beams with the lithium targets, provide an analysis of the neutron-flux/test-volume and test-volume/beam-current relationships, and describe the neutron-flux contours and the materials response functions in the test cell for various beam/target configurations.

4.1. Neutron Yield from Li(d, n) Reactions

Neutrons are generated in the lithium target primarily through the Li(d, n) stripping reaction, first analyzed by Serber,[9] but also by a variety of other nuclear processes. According to the Serber model, the neutrons produced in stripping have an energy

distribution given by

$$p(E_n) \, dE_n = \tfrac{1}{4}\pi R_d \frac{E_b(E_d - E_b)}{\left[(E_n - \tfrac{1}{2}E_d)^2 + E_b E_d\right]^{3/2}} \, dE_n$$

(1)

where R_d, E_b, and E_d are the deuteron radius, binding energy, and kinetic energy, respectively. The peak neutron energy is

$$E_{n(\text{peak})} = \tfrac{1}{2}\left[(E_d - (E_b + EB))\right]$$

(2)

with EB the Coulomb-barrier energy. The FWHM of the neutron energy distribution is

$$\Delta E_{\text{FWHM}} = 1.533\left[E_b(E_d - E_b - EB)\right]^{1/2}$$

(3)

For a deuteron energy of 35 MeV, Eqs. (2) and (3) yield

$$E_n(\text{peak}) = 15.2 \text{ MeV and } \Delta E_{\text{FWHM}} = 12.8 \text{ MeV}$$

for emission angles near 0°.

The angular distribution of the neutrons produced from the stripping reaction is given by

$$p(\theta) \, d\Omega$$

$$= \frac{R_d}{\pi} \frac{1}{\left[1 + (\theta/\theta_0)^2\right]^{3/2}}, \text{ with } \theta_0 = (E_b/E_d)^{1/2}$$

(4)

which is strongly forward-peaked, with an FWHM angle ($1.6\theta_0$) of approximately 23°.

To account for all significant neutron-producing processes in the Li(d, n) nuclear reactions, Serber's model has to be augmented. Two of the most important corrections are that:

1. At low deuteron energies ($E_d \leqslant 15$ MeV), a compound nucleus is formed, and neutrons are emitted isotropically with an energy distribution given by the classical evaporation model:

$$p(E_n) \, dE_n = E_n e^{-E_n/T}$$

(5)

where $T = 3.2\sqrt{E_d/A}$ is the compound-nucleus temperature and A is its mass.

2. High-energy neutrons ($E_n > E_d$) are produced by the exothermic reaction $^7\text{Li}(d, n)^8\text{Be}$ ($Q = 15.0$ MeV). This reaction yields neutrons with energies as
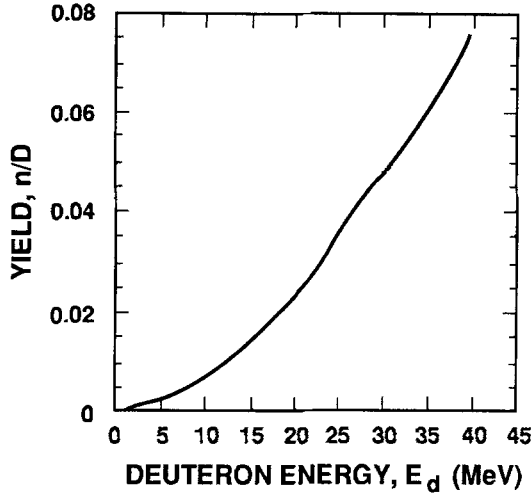
Fig. 12. Total neutron yield (neutrons per deuteron) vs. deuteron beam energy (from Ref. 12).

high as

$$E_{n,\max} = E_d + Q = 50 \text{ MeV}$$

The neutron yield of the lithium target (the number of neutrons produced per incident deuteron) must be estimated from experimental data, since the neutron-production cross-sections for the $Li(d, n)$ nuclear reactions as a function of energy are not completely known. Data from several research groups can be used to generate a semi-empirical functional dependence of the neutron yield on incident deuteron energy. Mann[12] has carried out a very detailed analysis of the existing data, and represents the $Li(d, n)$ thick-target-yield energy dependence by the curve shown in Fig. 12. This curve takes into account the corrections to the Serber model noted previously.

4.2. Neutron Source Function

The characteristics of the D-Lithium neutron source are determined by the beam current distribution (in the spatial and energy domains) at the lithium target and by the functional dependence of the $Li(d, n)$ reaction cross-sections on deuteron energy and neutron-emission angle. These characteristics govern the neutron flux, the neutron energy spectrum, and the energy deposition profile in the lithium jet (and thus the jet's thermal/hydraulic behavior).

To describe the beam spatial distribution, we use a coordinate system in which the x-direction is along the beam, the y-direction is parallel to the

lithium jet flow, and the z-direction is normal to both the beam direction and the jet flow. The origin is at the intersection of the beam axis with the target back wall. Along the lithium flow, the beam is assumed to have a Gaussian shape with an rms value (σ_y) of 1 cm. Perpendicular to the flow, the beam is modeled by a "split Gaussian" distribution, characterized by a 4-cm-wide flat top (δ) and Gaussian edges having rms values (σ_z) of 1 cm. The probability densities of the beam in the y- and z-directions are then:

$$f(y) = ce^{-1/2[y/\sigma_y]^2};$$

$$f(z) = \begin{cases} de^{-[(z+\delta/2)/\sigma_z]^2} & z < -\delta/2 \\ d & -\delta/2 \leq z \leq \delta/2 \quad (6) \\ de^{-[(z-\delta/2)/\sigma_z]^2} & z > \delta/2 \end{cases}$$

The normalization constants c and d can be calculated from

$$\int_{-\infty}^{+\infty} f(y) \, dy = 1 \text{ and } \int_{-\infty}^{+\infty} f(z) \, dz = 1,$$

which yield: $\quad c = \dfrac{1}{\sigma_y \sqrt{2\pi}} \text{ and } d = \dfrac{1}{\delta + \sigma_z \sqrt{2\pi}} \quad (7)$

Using Eqs. (6) and (7), and representing the beam density distribution in the y-direction as a Gaussian, one can write the two-dimensional (y, z) current density on target as

$$J(y, z) = I_{tot} \left[\frac{1}{\sigma_y \sqrt{2\pi}} e^{-1/2[y/\sigma_y]^2} \frac{1}{\delta + \sigma_z \sqrt{2\pi}} \right. $$

$$\left. \times \begin{cases} e^{-1/2[(z+\delta/2)/\sigma_z]^2} & z < -\delta/2 \\ 1 & -\delta/2 \leq z \leq \delta/2 \\ e^{-1/2[(z-\delta/2)/\sigma_z]^2} & z > \delta/2 \end{cases} \right] \quad (8)$$

where I_{tot} is the total beam current (mA).

Figure 13 provides a graphical display of the model (x, z) current density profile, for the values of δ, σ_y, and σ_z given. For the reference (250-mA) beam the maximum current density (at $y = 0, -2 \leq z \leq 2$) is only 15.3 mA/cm². For comparison, the maximum current density estimated for the FMIT target was 29 mA/cm². The FMIT beam-density distribution was Gaussian in both planes, with 1 cm FWHM in the
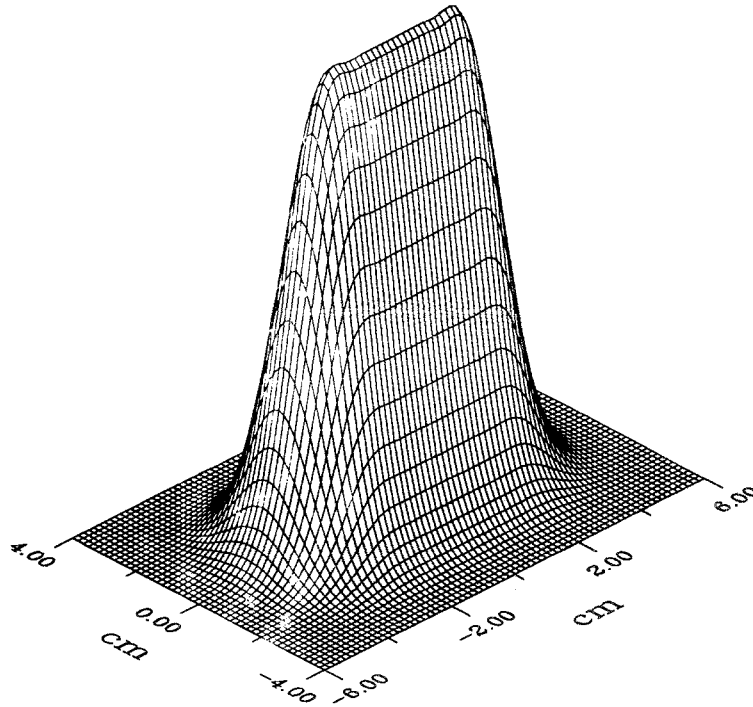
Fig. 13. Two-dimensional current-density profile for the reference beam at the lithium target.

y-direction and 3 cm FWHM in the *z*-direction. Therefore, although the beam intensity per target in the present design is 2.5 times greater than for FMIT, the broader (*y* and *z*) and flatter (*z*) current distributions yield a factor-of-2 lower peak current density.

In the energy domain, the beam emerging from the accelerator has an (approximately) Gaussian density distribution with an rms spread of $\sigma_E \cong 70$ keV. As noted in Section 2, a combination of space-charge forces and an energy-dispersion rf cavity cause the rms value of the energy distribution to grow to 1.0 MeV by the time the beam strikes the lithium target. The target is thick enough (about 2.0 cm) to completely stop the deuterons, so the neutron yield must be estimated for the entire range of deuteron energies, from 35 MeV down to the neutron-production threshold.

4.3. Flux Calculations

A critical design objective of the D-Lithium neutron source is to provide large test volumes at neutron flux levels high enough to simulate a range of fusion-reactor conditions. The neutron flux at any position in the test cell is given by the integral:

$$\frac{d\Phi(E_n)}{dE_n} = N \int_0^{E_d} \int_{y} \int_{z} \frac{d^2\sigma(E_d, E_n, \theta)}{dE_n \, d\Omega} \frac{J(y, z)}{e}$$

$$\times \frac{dE_d}{r^2[dE_d/dx]} \, dy \, dz \qquad (9)$$

where the x, y, z coordinate system is as specified here, with $J(y, z)$ = two-dimensional current density profile of the deuteron beam, e = electronic charge, N = atomic density of lithium, dE_d/dx = energy-dependent stopping power of deuterons in lithium,

$$\frac{d^2\sigma(E_d, E_n, \theta)}{dE_n \, d\Omega}$$

= differential cross-section for deuterons of energy E_d, to produce neutrons of energy E_n at an emission angle θ, and r = distance from the neutron-production point to the test cell sample position.

Integration over the *x*-direction in Eq. (9) is replaced by integration over the deuteron energy, using the relation between deuteron stopping power and energy. The differential cross-section cannot be determined analytically, since it involves a combina-

tion of contributions from classical nuclear stripping theory, the compound-nucleus evaporation model, and other nuclear reactions, as indicated previously. Unfortunately, differential cross-section measurements exist for only a few deuteron energies and for only a few neutron-emission angles. Mann *et al.*[12] fitted all the existing data and was able to project useful semi-empirical curves for the differential cross-section over the deuteron-energy range of interest. These fits are used to generate a complete differential cross-section table that can be employed with Eq. (9) to numerically calculate the neutron flux at all points within the test cell.

We determined the uncollided neutron flux (integrated over energy) for a grid of points within the test cell, and then estimated the volumes enclosing regions having specific average flux values. The flux level was converted to an equivalent 14.1-MeV neutron-wall-loading power to allow direct comparison with fusion-reactor parameters. Results of these flux/volume calculations for different deuteron current levels are summarized in Fig. 14.

The figure succinctly demonstrates the capabilities of the D-Lithium source for fusion-materials testing. For the reference design (two 250-mA beams), test volumes exceeding 10 liters can be achieved with equivalent wall loadings of 1–4 MW/m², the flux level of greatest interest for fusion-reactor damage simulation. From inspection of the figure, we see that below 20 MW/m², there are approximately exponential connections between available test volumes and

average wall-loading power. A regression analysis yields the following exponential relations, which can be used to obtain quick estimates of available test volumes at specific average wall loadings, for several (total) beam currents:

$$V(\text{liters}) = 21.9 \text{ WL}^{-2.22} \ (\text{MW}/\text{m}^2) \quad (I = 125 \text{ mA})$$

$$V(\text{liters}) = 55.4 \text{ WL}^{-1.99} \ (\text{MW}/\text{m}^2) \quad (I = 250 \text{ mA})$$

$$V(\text{liters}) = 175.1 \text{ WL}^{-1.94} \ (\text{MW}/\text{m}^2) \quad (I = 500 \text{ mA})$$

$$(10)$$

From the neutron-flux maps, one can alternatively calculate the available test volumes at specific beam currents for various average wall loadings. Results are summarized in Fig. 15 for wall loadings of 1, 5, 10, and 15 MW/m². The curve for the 1-MW/m² level is obtained by an extrapolation of the data and should be viewed as only indicative. A regression analysis performed on these curves yields the exponential relations:

$$V(\text{liters}) = 27.791 \ I^{1.83} \ (\text{A}) \quad (\text{WL} = 5 \text{ MW}/\text{m}^2)$$

$$V(\text{liters}) = 8.164 \ I^{1.97} \ (\text{A}) \quad (\text{WL} = 10 \text{ MW}/\text{m}^2)$$

$$V(\text{liters}) = 3.995 \ I^{2.05} \ (\text{A}) \quad (\text{WL} = 15 \text{ MW}/\text{m}^2)$$
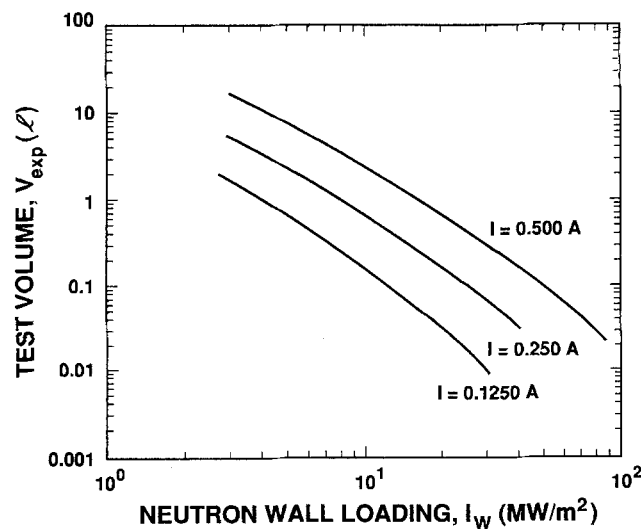
$$(11)$$

Fig. 14. Volume (liters) vs. equivalent uncollided neutron wall-loading power, for three different deuteron beam currents.
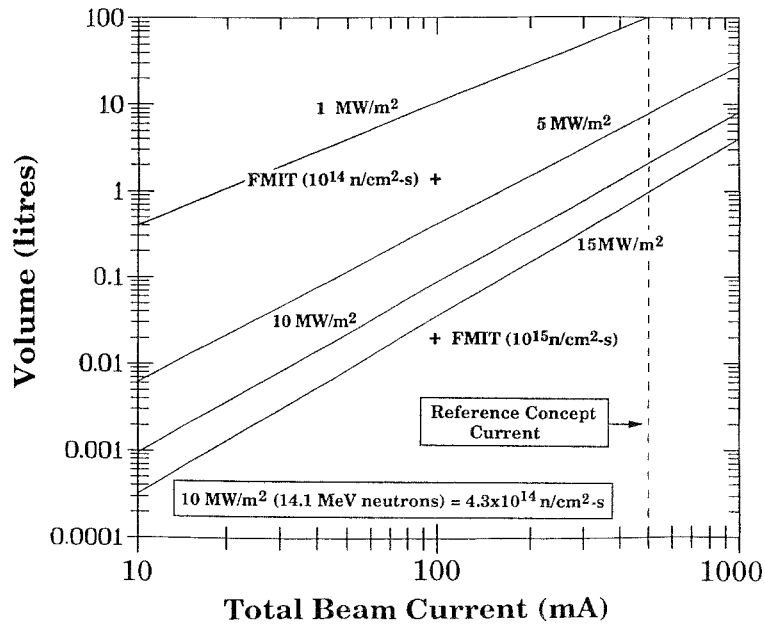
Fig. 15. Available test volume (liters) vs. deuteron beam current for various wall-loading levels.

Because the value of the exponent is close to two, the test volume at a given average flux grows nearly quadratically with the total beam current, and the benefit (for large-component testing) inherent in scaling to higher currents is dramatic. For example, a factor of 4 increase in current improves the test volume at a given flux level by nearly a factor of 16.

Figure 15 allows us to make a reasonable projection of the test volume available at both very low and very high beam currents. About a 1-liter volume can be obtained at an average wall loading of 1 MW/m² with a beam current as low as 25 mA. On the other end of the scale, test volumes of a few-hundred liters

at average wall loadings of 1 MW/m² could be achieved with a D-Lithium source configured with two 500-mA beams. Such an "ultimate" system could also provide a 20-liter test volume at 5 MW/m² average wall loading. These comments illustrate the great range of neutron flux and test volume trade-offs that are attainable with the proposed D-Lithium source.

4.4. Flux Contour Optimization

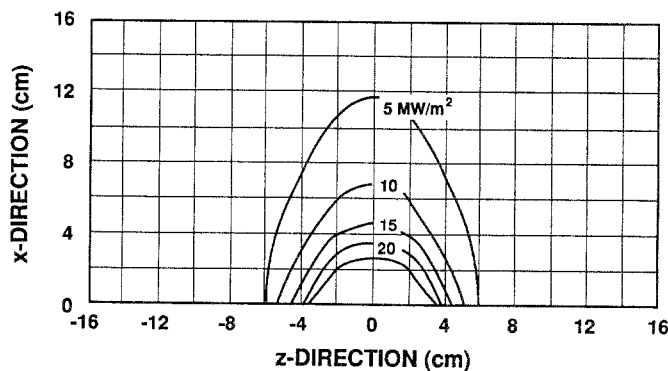A very important qualitative difference between the source design proposed here and FMIT is the

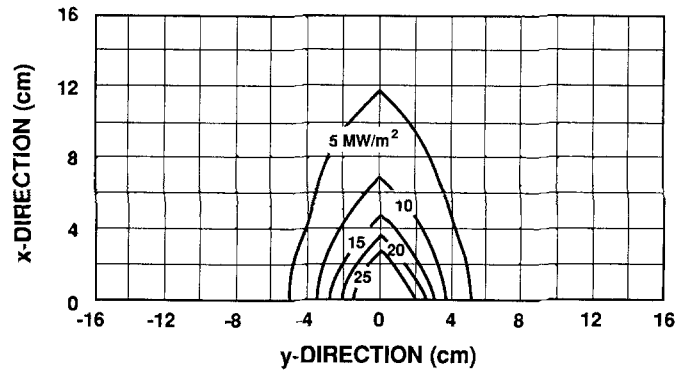Fig. 16. Wall-loading contour for the (x-z) plane from one 250-mA beam on one target.

Fig. 17. Wall-loading contour for the (x-y) plane from one 250-mA beam on one target.

two-target configuration. This section assesses the implications of the dual-source geometry in terms of (uncollided) neutron-flux contour maps of the test region. For all the cases presented, the uncollided flux is transformed into an equivalent 14.1-MeV-neutron wall-loading power.

Figures 16 and 17 show the neutron-flux contours in the planes [(x-z) and (x-y)] that characterize the neutron field generated by a single beam incident on a single target. The coordinate system is the same as previously used, and the maps are at z = 0 and y = 0 in these two orthogonal cuts. A comparison of the figures indicates similar shapes for the equal-flux contours, with a broader width in the (x-z) plane, due to the "split-Gaussian" beam distribution. The 1-MW/m² wall-loading level extends to about ±16

cm in the y and z directions, and to about +30 cm in the x direction.

The critical parameters for the two-target geometry are the relative orientation angle of the targets, and the distance from their common vertex. Figure 18 shows an (x-z) plane flux-contour map for the reference design, in which 250-mA beams are incident on two targets oriented at 90° and centered 10 cm from their common vertex. This map was produced by simple superposition of two contour plots identical to the one of Fig. 16. The main topological features that are evident in Fig. 18 are (1) relatively large regions of low flux gradient and moderate wall loading in the center of the test cell, (2) small regions (≈100 cm³) with very high wall loading (>15 MW/m²) and high flux gradient close to the lithium
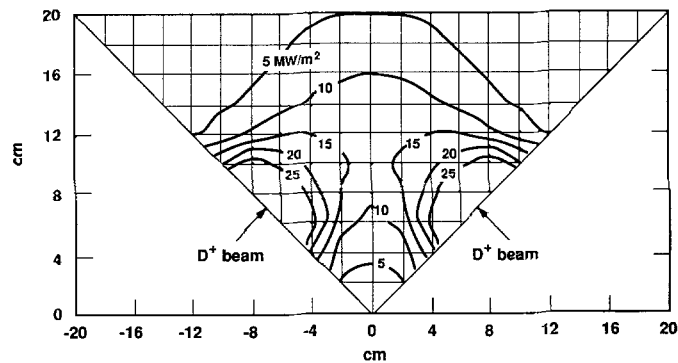

Fig. 18. Neutron wall-loading-power contour plot for two 250-mA beams and two lithium targets at relative orientation of 90° and spaced 10 cm from vertex.
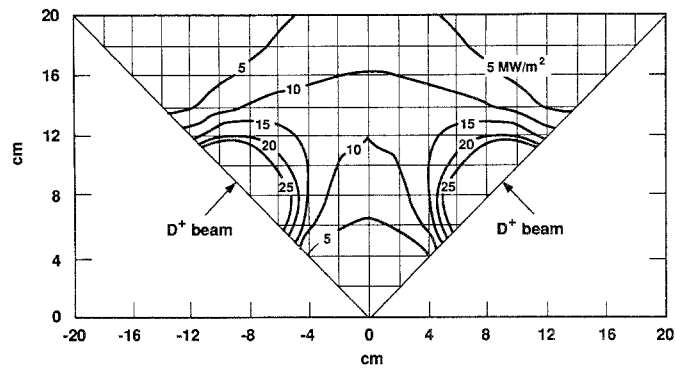
Fig. 19. Neutron wall-loading-power contour plot for two 250-mA beams and two lithium targets at relative orientation of 90° and spaced 12 cm from vertex.

targets, and (3) a large range of wall loadings (<1 MW/m² up to > 25 MW/m²) at different parts of the test zone in which small materials specimens could be exposed simultaneously.

Figures 19–21 show the neutron-flux contours generated by two 250-mA beams for target orientations and/or spacings differing from the reference geometry. The flux map of Fig. 19 is generated by targets oriented at 90° but centered 12 cm from their common vertex. Figures 20 and 21 show flux maps for targets centered 10 cm from the vertex, but having 120° and 60° relative orientations, respectively.

A careful inspection of Figs. 18–21 prompts the following general observations. Increased target spac-

ing enlarges the test volume for low-to-medium wall loadings (1–10 MW/m²), but reduces the test volume for high wall loadings (15–20 MW/m²). As target orientation angles increase, the neutron-flux gradients are significantly reduced and the test volume at low-to-medium flux levels is enlarged. As target orientation angles decrease, flux gradients become steep, but the available test volume at high wall loadings greatly increases. If either target spacing or angular orientation are increased too much, the system separates into two independent (non-overlapping) neutron plumes, decreasing the effective test volume available at medium-flux levels. Thus, we see that test-region neutron-flux gradients and volume/flux ratios can be tailored to suit different user
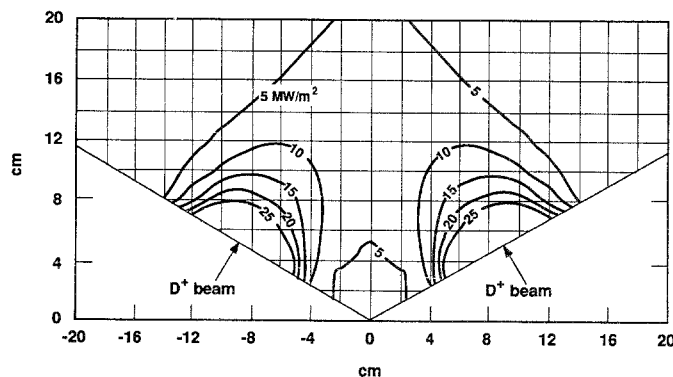

Fig. 20. Neutron wall-loading-power contour plot for two 250-mA beams, and two lithium targets at relative orientation of 120° and spaced 10 cm from vertex.
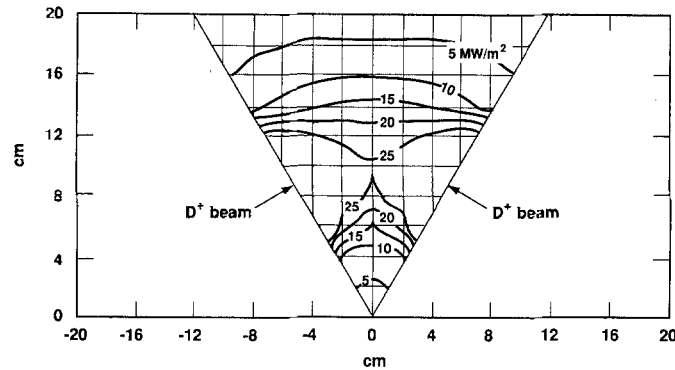
Fig. 21. Neutron wall-loading-power contour plot for two 250-mA beams, and two lithium targets at relative orientation of 60° and spaced 10 cm from vertex.

requirements by varying the controlling target parameters (orientation and spacing) over a limited range of values.

4.5. Materials Response Functions; Spectrum Dependence

Neutrons produced in the thick lithium target have a rather broad energy spectrum, and the spectrum shape varies with emission angle and distance from the target. At forward angles and distances not too close to the target, the spectrum is dominated by the stripping reaction, and has a well-defined peak at about half the beam energy. However, at large emission angles and at distances close to the target, the stripping peak is less prominent, and the spectrum contains a higher proportion of lower-energy (few MeV) evaporation neutrons. Also, as noted earlier, the 35-MeV deuterons produce a tail of higher-energy neutrons up to 50 MeV.[12] It is important to estimate the response functions of test materials exposed to the relatively broad D-Lithium source spectrum and compare them with those expected from a fusion-reactor first-wall neutron spectrum. The analysis that follows is based on the uncollided neutron spatial and spectral distributions produced by a 250-mA beam incident on a single lithium target.

Figure 22 shows the uncollided neutron flux as a function of energy at various positions (x, y, z) within the test region, using the beam/target coordinate system defined in Section 4.2. Position $(0,0,0)$ is at the center of the target back plate, and is the point of maximum neutron flux. The high-energy neutron tail is clearly visible at this location, but only 15% of the neutrons have energies above 14 MeV. In most other
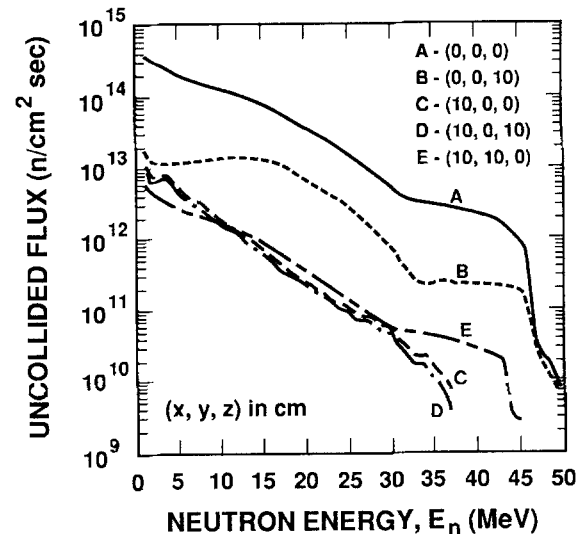
Fig. 22. Uncollided neutron-flux spectrum at various positions within the test-cell region.

test-cell locations, the high-energy component of the spectrum contains a smaller fraction of the total neutron flux.

The response functions typically used to characterize neutron-induced damage in materials are the number of displacements per atom per year (dpa/yr) and the production rate of helium (appm/yr). Detailed damage cross-section data up to neutron energies of 50 MeV are needed for a comprehensive assessment of the relative importance of spectral differences between the D-Lithium source and the expected fusion neutron environment. Unfortunately, such data do not exist for most materials of interest. Our analysis is therefore limited to copper, for which

suitably detailed measurements have been made. Figure 23 shows the damage cross-section data for copper over the neutron energy range from 1 to 50 MeV.

From the information in Figs. 22 and 23, we can calculate the materials response ratios
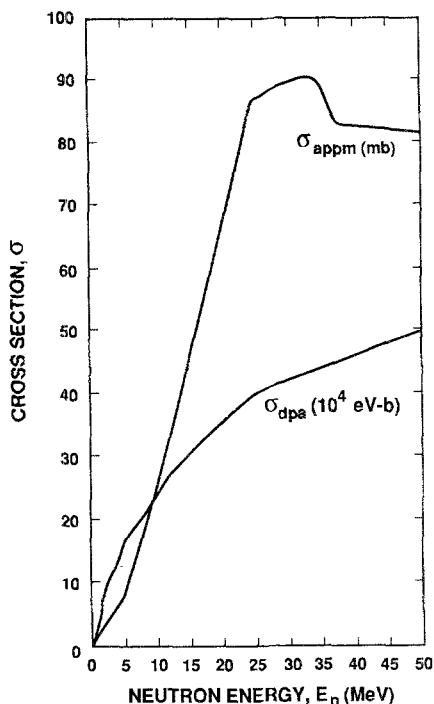
$$\frac{dpa/yr}{MW/m^2} \quad and \quad \frac{appm/yr}{dpa/yr}$$

Fig. 23. Damage cross-section data for copper (σ_{dpa} in 10^4 eV-b, and σ_{appm} in mb).

for copper samples exposed to the D-Lithium neutron source, as a function of position in the test region. The resulting maps of these two quantities are shown in Figs. 24 and 25, respectively. The calculation was carried out in the $(x\text{-}z)$ plane within a region spanning ± 20 cm from $z = 0$, and $+20$ cm from $x = 0$.

Figure 24 reveals that the damage rate per unit of wall-loading power is relatively insensitive to position in the test region, and by inference to the spectrum variation. The maximum variation of this parameter over the entire region is about a factor of two. The variation is as low as 10% within a large zone in the forward direction. Figure 25 shows that the important ratio of appm/yr to dpa/yr is constant within 10% over a large forward-angle zone, but decreases by up to a factor of 2 at large angles, where the neutron spectrum is very different from that near $0°$. These maps indicate that exact sample positioning is not very critical for damage measurements made within the forward-angle region, and, on the other hand, that spectrum effects could be evaluated by moving test samples from the forward-angle region to a high-angle region of the test cell.

Table III lists the variation range of the materials response functions plotted in Figs. 24 and 25, and compares them with the values estimated for a first-wall fusion source. The table shows clearly that damage in copper from D-Lithium source neutrons brackets the damage that would arise from fusion first-wall neutrons, demonstrating that the high-energy tail produced by the D-Lithium source has minimal impact on its effectiveness as a fusion-spectrum simulator. Table III also lists the maximum
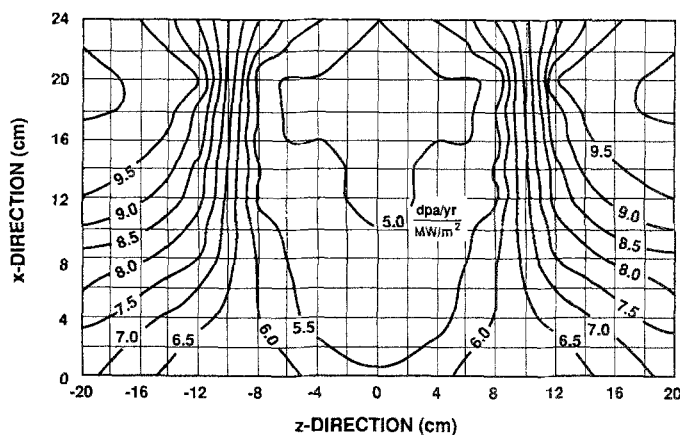

Fig. 24. dpa/yr per (uncollided) MW/m^2 on copper produced by the neutrons from a 250-mA D-Lithium source.

Table III. Comparison of Radiation Damage Produced by Neutrons from a 250-mA D-Lithium Source and from a Fusion First-Wall Spectrum[a]

	D-lithium	Fusion FW
Max dpa/yr	220	
Max appm/yr	1950	
appm/yr/dpa/yr	6–12	≈ 7.4
dpa/yr/MW/m²	5–10	7–10

[a]Damage on copper.

damage rates available in the D-Lithium source test cell, for specimens placed close to the target. These rates are very high, and would permit accelerated testing of small samples.

5. TARGET ENGINEERING ANALYSIS

This section discusses thermal management of the beam power deposited in the lithium jet targets. At a current of 250 mA per beam, the total power deposited in each jet by 35-MeV deuterons is nearly 8.75 MW. The analysis is separated into (1) consideration of the deuteron energy-deposition profile, and (2) the thermal/hydraulics of the heated jet. The interaction of the high-power deuteron beam with the flowing lithium produces high local rates of energy deposition in the jet, causing high temperatures. The purpose of the analysis described here is to determine the temperature distribution of the jet in

steady-state operation and to assess whether the temperature maximum is safely below the saturated vapor temperature (boiling point) at all points in the jet.

5.1. Energy-Deposition in Lithium

The passage of a charged particle through matter is characterized by the rate of energy loss along its path through Coulomb interactions with atomic electrons, a phenomenon studied extensively by Bethe[13] and Fano.[14] Our analysis used the Monte Carlo code TRIM (TRansport of Ions in Matter)[15] to generate and sum the collision histories of a large number of deuterons slowing down in lithium. These histories, which start with specified particle energy, position, and direction, include angle changes caused by nuclear collisions and energy changes resulting from nuclear and electronic interactions. They are terminated when the deuteron energy drops below a specified level or when the particle leaves the target. TRIM was used to estimate the energy-loss profile (energy-loss rate vs. energy) of deuterons have initial energies ranging from 13 MeV to 37 MeV, slowing down in liquid lithium of density 0.51 g/cm³. Results are shown in Fig. 26, which illustrates how the deuteron range in lithium decreases and the maximum energy-loss rate increases as the incident deuteron energy decreases. The mean range (R_m) and maximum energy loss rate $[(dE/dx)_{max}]$ can be
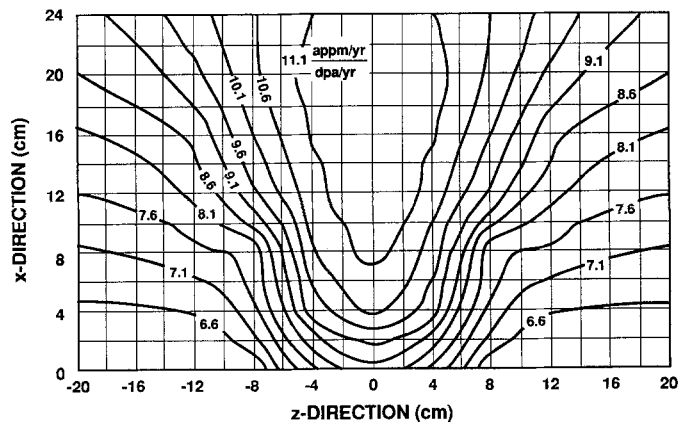
Fig. 25. Ratio of appm/yr over dpa/yr for copper produced by the neutrons from a 250-mA D-Lithium source.
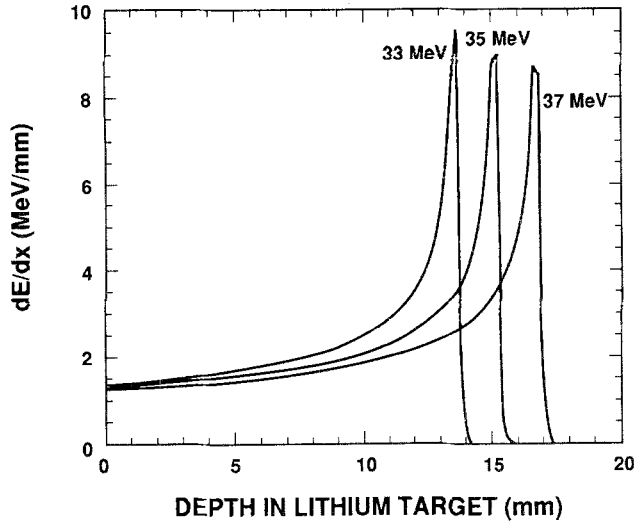
Fig. 26. Energy-loss profile for deuterons on lithium, as calculated by TRIM.

Fig. 27. Energy-loss profile for 35-MeV deuterons on lithium: (A) mono-energetic beam, (B) Gaussian beam with $\sigma_E = 1$ MeV.

accurately fitted by the exponential formulas

$$R_m(\text{mm}) = 0.025 E_d^{1.806}(\text{MeV}) \qquad (12)$$

$$\left(\frac{dE}{dx}\right)_{max}\left(\frac{\text{MeV}}{\text{mm}}\right) = 73.127 E_d^{-0.578}(\text{MeV}) \qquad (13)$$

A direct inference is that deuteron currents for lower beam energies would have to be significantly less than those at 35 MeV to preserve adequate safety margins against local boiling in the lithium jet.

The effect of finite energy spread in the deuteron beam is of major importance in reducing the peak energy deposition in the target. The beam produced by the accelerator and HEBT is not mono-energetic, but has a Gaussian energy distribution with an rms width of 1.0 MeV. The energy-loss profile in the target for this beam was estimated by splitting it into 1/2-MeV energy bins, and then summing individual energy-loss contributions weighted by the beam energy-distribution function.

The calculation results are summarized in Fig. 27, which compares the energy-loss profile of a mono-energetic 35-MeV beam and a 35-MeV beam with a 1.0-MeV rms width. We see that the latter yields an energy-loss profile having a maximum only 1/2 that of the former (4.6 MeV/mm vs. 9.1 MeV/mm). The above analysis was repeated for beams with mean energies of 15 MeV, 20 MeV, 25 MeV, and 30 MeV. The dependence of maximum energy-loss rate on incident deuteron energy can be
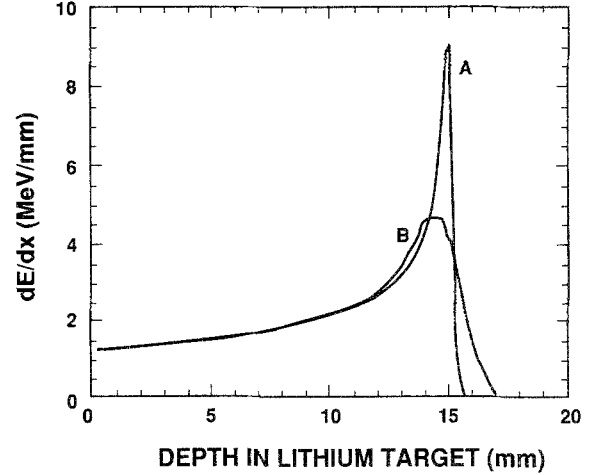
represented by the exponential relationship

$$\left(\frac{dE}{dx}\right)_{max}\left(\frac{\text{MeV}}{\text{mm}}\right) = 29.5 E^{-0.52}(\text{MeV}) \qquad (14)$$

5.2. Thermal/Hydraulic Analysis

The input flow conditions (temperature and velocity) assumed for the jet thermal/hydraulic analysis are the same as those used for FMIT.[16] Liquid lithium at a bulk temperature of 220°C is accelerated vertically downward by a nozzle of rectangular cross-section, to an average velocity of 17.3 m/s. As noted earlier, the rear jet surface moves along a 1.6-mm thick curved steel wall, and the front surface is exposed to the deuteron beam and the HEBT vacuum at a pressure of 10^{-6} Torr. The jet thickness at the nozzle exit is 1.9 cm, its width in the z-direction is 10 cm, and the radius of curvature of the wall is 11 cm. The center line of the beam is 12 cm below the exit of the nozzle, at $y = 0$. Figure 28 shows a section through the beam/jet intersection region.

The numerical procedure used to perform the thermal/hydraulic calculations is an adaptation of the Patankar-Spalding (PK) method.[17] It is an implicit finite-difference marching procedure capable of handling both wall boundaries and free boundaries. The lithium jet can be considered as a kind of boundary-layer flow because velocity and temperature gradients are much larger in the cross-stream direction than in the flow direction. We assumed that downstream perturbations do not significantly affect upstream conditions. We also supposed generally
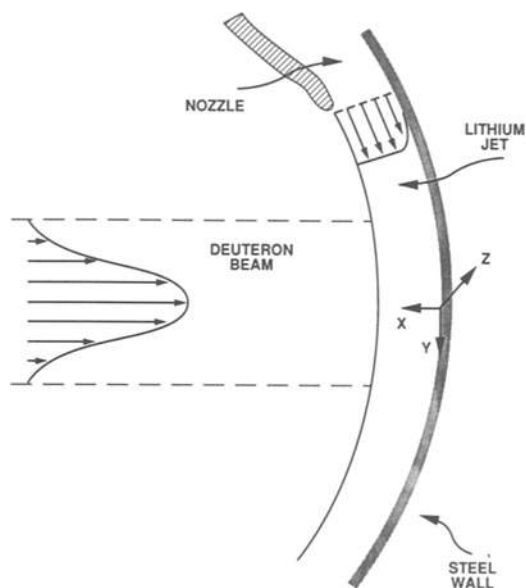
Fig. 28. Schematic of the lithium jet used for thermal/hydraulic calculations. Relative dimensions of beam and target are not to scale.

Fig. 29. Back-wall heat-flux distribution for the reference beam.

stable (non-turbulent) flow conditions in the jet, an assumption justified by several studies[16,18] that considered possible instability mechanisms and showed them to present no significant threat.

A complete system of energy and momentum equations is solved, for the case of steady flow, by an implicit marching procedure subject to appropriate boundary conditions. The first step is to specify initial x-direction positions of N cross-stream nodes at the exit of the jet nozzle ($y = +12$ cm). We choose $N = 120$, and use a non-uniform x-spacing, with much closer spacing near the wall to obtain sufficient accuracy in the boundary layer. Initial jet profiles are specified using a 1/7 power law distribution for velocity and a uniform distribution for enthalpy. Then a small downstream step (Δy) is taken and new velocity and enthalpy profiles are computed. The independent variable for these calculations is the stream function. The boundary conditions for the velocity calculation are $u = 0$ at the wall and $\partial u / \partial x = 0$ at the free surface. The downstream pressure gradient is zero. The thermal boundary conditions are $\partial h / \partial x = 0$ at the free surface and the heat flux at the target wall ($x = 0$, y, z).

After a new enthalpy profile is found, new values of temperature, density, viscosity, and Prandtl number are found from property tables[19]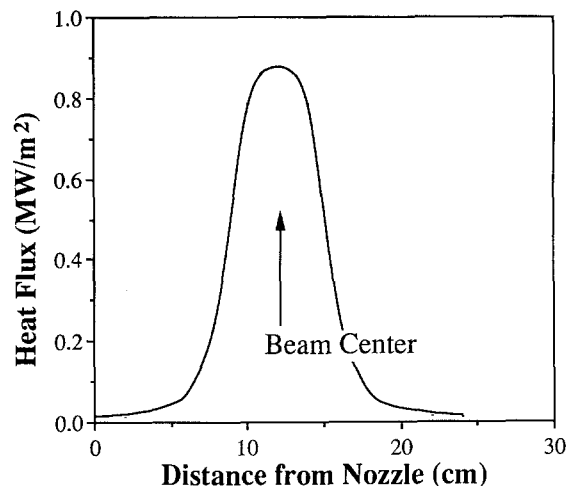 incorporated into the code. The updated property values are used for the next calculation step. The cross-stream pressure profile is found by integrating the centrifugal force effect caused by the curved target surface. The local values of saturation temperature can then be calculated for comparison to the local jet temperature to determine whether boiling can occur.

Significant energy is deposited within the target back wall by neutron absorption. Assuming negligible heat radiated from the wall surface facing the test region, this energy is transferred by conduction to the flowing lithium. The heat-flux distribution at the lithium-facing wall surface, calculated from the neutron-flux contours of Fig. 16 is shown in Fig. 29.

The reference case for the calculation is a 250-mA deuteron beam incident on a jet target with input parameters described above. The flow-direction step size used in the computation is 0.1 mm. The beam energy-deposition profile (Fig. 27) is folded with the two-dimensional beam spatial-density distribution (Fig. 13) to obtain the three-dimensional volumetric energy-deposition rate in the lithium at all (x, y, z) points within the beam/target intersection. This function and the heat flux from the target wall (Fig. 29), which depends on y and z, are the thermal inputs to the thermal/hydraulic calculation of the jet performance.

General results of the PK calculations for our reference model are summarized in Figs. 30–33. Figure 30 shows that the jet thickness increases by about 14% as the lithium passes through the beam. This is caused by the density decrease that occurs with increasing temperature and also by a slight decrease in local velocity near the wall (which is independent of
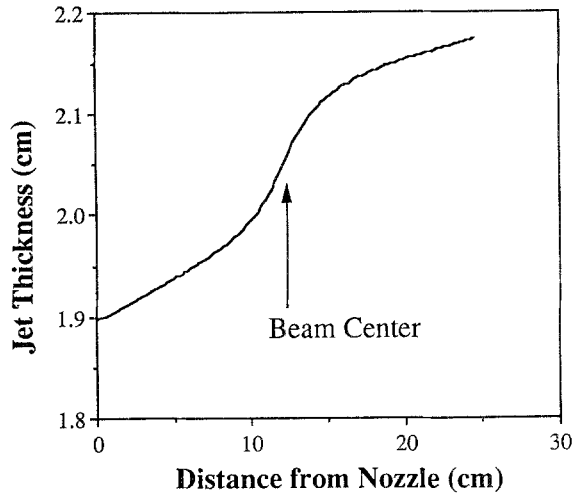
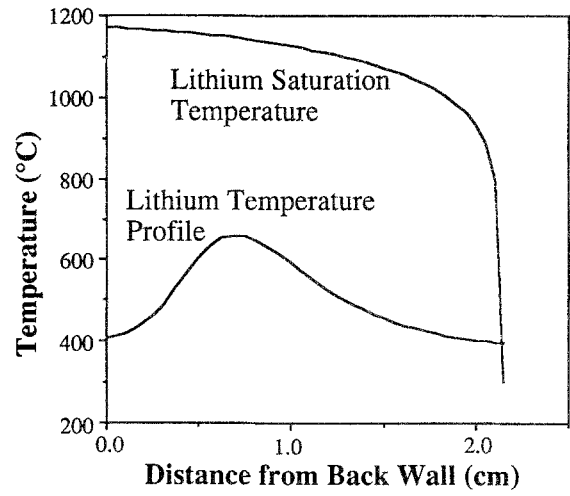**Fig. 30.** Lithium-jet thickness growth for 250-mA beam.

Fig. 32. Comparison of (maximum-temperature) lithium-jet temperature profile and local saturation-temperature profile for 250-mA beam.
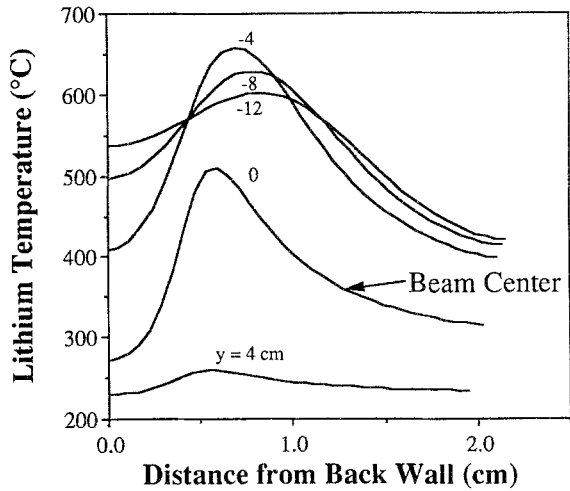
Fig. 31. Lithium-jet temperature profiles for 250-mA beam. Positive (negative) y values represent upstream (downstream) positions relative to beam axis.
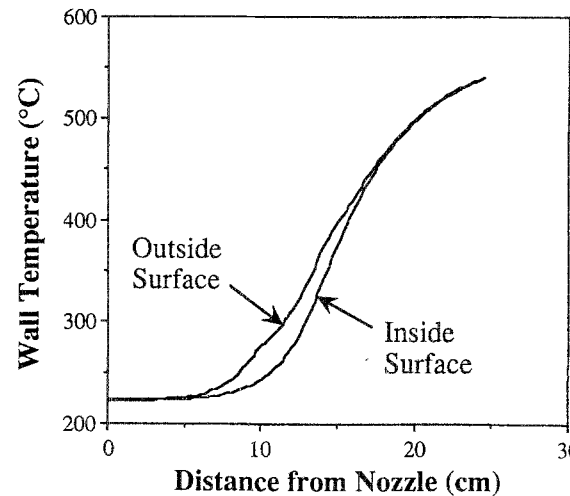
Fig. 33. Back-wall temperature profiles for 250-mA beam. Inside surface is in contact with lithium jet; outside surface faces test region.

the jet heating by the beam). Temperature profiles in the lithium at five downstream distances (y) from the nozzle are shown in Fig. 31. Most of the energy is deposited in the range $+4 \geqslant y \geqslant -4$ cm. The maximum lithium temperature (660°C) occurs 4-cm below the beam axis and 0.7 cm from the back wall. At greater downstream distances, the average (bulk) temperature at each (x-z) plane section in the jet continues to rise, but the peak temperature decreases, because of cross-stream diffusion.

A comparison of the lithium temperature profile in the (x-z) plane containing the highest lithium temperature with the lithium saturation-temperature

profile (boiling point) in that plane is shown in Fig. 32. The fluid temperature remains safely below the saturation temperature, except for a very narrow region at the free surface of the jet, where the pressure approaches 10^{-6} Torr.

Some lithium evaporation will occur at the free surface, and we can estimate it using kinetic theory, with the equation

$$\Gamma = \left(A/8R' \right)^{1/2} \left(P/T^{1/2} \right) \text{ (kg/s)} \qquad (15)$$

where A is the atomic number of lithium, $R' = 8317$ J/kg-mole-K is the universal gas constant, T is the lithium surface temperature, and P is the saturation pressure at that temperature. Equation (15) is numerically integrated in the code along the jet flow direction. The evaporation rate for the reference case is 6.4×10^{-5} g/s (5.5 g/day), for a total jet width (z-direction) of 10 cm. This rate is insignificant as far as loss of material from the lithium circulation system is concerned. It is large enough to pose a contamination threat to the HEBT vacuum system, but can easily be collected on an upstream cold trap and removed during scheduled maintenance periods.

The calculated target-wall temperatures are shown in Fig. 33. The inside surface temperature is equal to the lithium temperature at $x = 0$. The outside surface temperature is calculated from

$$T_o = T_i + q_f(\tau/2k) \tag{16}$$

where T_i is the inside surface temperature, q_f is the local heat flux, τ is the wall thickness, and k is the thermal conductivity of the wall material (304 stainless steel). The maximum temperature of 540°C is well below the softening temperature of the steel.

Thermal/hydraulic calculations were performed for beam currents (on one target) of 125 mA and 500 mA, as well as for the reference case, using the jet velocity assumed earlier. A final calculation at 500 mA was made with a higher jet velocity (19.0 m/s). The minimum boiling temperature margin, T_{mb}, defined as the minimum difference between the saturation temperature and local lithium temperature at any point in the flow field (not including the thin free-surface layer) was calculated for each case, as

Table IV. Dependence of Lithium Evaporation Rate (Γ) and Boiling Margin (T_{mb}) on Beam Current and Jet Velocity

I (mA)	V (m/s)	Γ (kg/s)	T_{mb} (°C)
125.0	17.3	8.5×10^{-10}	566.1
250.0	17.3	6.4×10^{-8}	466.1
500.0	17.3	2.3×10^{-5}	43.6
500.0	19.0	9.7×10^{-6}	143.1

was the lithium evaporation rate at the free surface. Results of these calculations are summarized in Table IV. We see that the evaporation rate increases extremely rapidly with increasing beam current, and that at 500 mA a significant lithium recovery problem could arise. At this level of beam current and a jet velocity of 17.3 m/s, T_{mb} falls to an unacceptably small value. However, the surface evaporation rate can be reduced and the boiling margin can be increased by sizeable factors (2–4) if the jet velocity is raised by a relatively modest amount (to 19.0 m/s).

Lower maximum target temperatures were obtained in the present calculations (in spite of the higher beam current) than in those carried out previously for FMIT.[16] The two main reasons for this result are that (1) the earlier calculation did not account for lateral heat flow (across the jet flow) which significantly reduces the peak local temperature, and (2) the beam-current densities at the target are actually lower than for FMIT because of the wider and flatter (x-z) plane distribution. Table V summarizes the overall results of the present target performance analysis, and compares them with those of the FMIT design.

Table V. Comparison of Thermal/Hydraulic Calculation Results for New D-Lithium Concept and for FMIT Design

	New concept			FMIT
Beam current profile				
Along flow	Gaussian ($\sigma = 1$ cm)			Gaussian ($\sigma = 1$ cm)
Perpendicular to flow	Split Gaussian ($\sigma = 1$ cm, $\delta = 4$ cm)			Gaussian ($\sigma = 3$ cm)
Current (mA)	125	250	500	100
Beam energy (MeV)	35	35	35	35
Beam energy spread (MeV)	1.0	1.0	1.0	0.5
$(dE/dx)_{max}$ (MeV/mm)	4.6	4.6	4.6	6.0
J_{max} (mA/cm^2)	7.7	15.4	30.7	29
P_{max} (MW/cm^3)	0.35	0.70	1.41	1.74
Velocity (m/s)	17.3	17.3	19.0	17.0
Jet inlet temperature (°C)	220	220	220	220
Jet maximum temperature (°C)	451	672	1017	820
Minimum boiling margin (°C)	566	466	143	300
Surface evaporation (kg/s)	8.5×10^{-10}	6.4×10^{-8}	9.7×10^{-6}	4.5×10^{-10}
Mass flow rate (kg/m-s)	8750	8750	9741	

6. COST ESTIMATES AND FIGURE OF MERIT

This section provides construction- and operating-cost estimates for a D-Lithium neutron source for a range of deuteron currents. A cost-effectiveness comparison with an existing fission-neutron materials testing source is also presented.

6.1. Cost Estimates

A preliminary analysis of construction and operating costs has been carried out for a D-Lithium neutron source at several deuteron current levels. Construction costs (presented in 1989 $U.S.) are summarized in Table VI. The accelerator estimates are based on recent component costs, while target and test-facility costs are estimated using scalings from FMIT. Costs are tabulated for total facility currents of 125 mA, 250 mA, 500 mA (the reference concept), and 1000 mA. Accelerator- and HEBT-configuration assumptions for each case are indicated in the table footnotes. The estimated construction cost for the reference concept ($232.4 million) is close to the 1984 FMIT facility construction estimate of $180 million when escalation at 5% per year is included. However, the concept proposed here would have five times the FMIT deuteron current and 20 times the useful test volume at specific neutron-flux levels.

The cost scaling with beam current is given in Fig. 34, and can be approximated reasonably well by
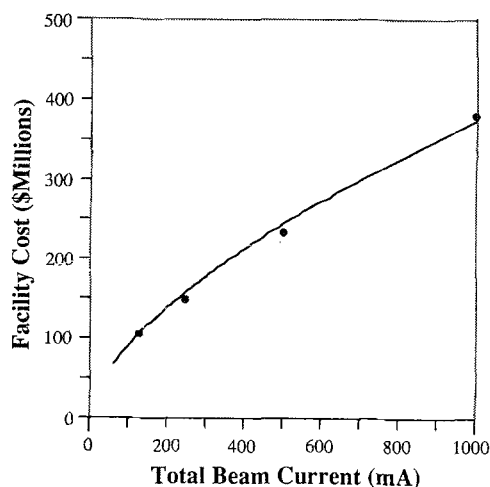

Fig. 34. D-Lithium neutron-source construction cost estimate vs. total beam current.

the relation

$$\text{Cost(M\$)} = 5.15(I_d)^{0.62} \qquad (17)$$

where I_d is the total current in mA.

Annual operating cost estimates for D-Lithium neutron sources with the same values of total beam current as in Table VI are summarized in Table VII. Electric-power costs assume 85% beam-on time, conventional ac/rf power-conversion efficiency (0.46), and an electrical line source as economical as that planned for FMIT ($0.035/kW-hr). The fraction of total operating costs required to cover electric power requirements ranges from 0.38 at 125 mA to 0.64 at 1000 mA.

6.2. Figure-of-Merit Evaluation

A relative-figure-of-merit (RFOM) evaluation has been suggested[20] that would permit a performance comparison between various proposed fusion-technology neutron sources. This procedure has been used elsewhere to evaluate the performance of a Reversed-Field Pinch[20] neutron source and a Dense Z-Pinch[21] neutron source, and is used here to evaluate the comparative performance of the reference D-Lithium source. An RFOM value of 1.0 for a neutron source is defined as equivalent to a cost of 20 M$/dpa/yr-m^3, which is the present dollar cost of generating unit damage per unit time in a unit volume (dpa/yr-m^3) of test material at the Fast-Flux Test Facility (FFTF). Lower values of RFOM mean lower unit testing costs. The reasons for selecting the FFTF as the baseline facility, despite the fact that its neutron spectrum is substantially different from a fusion first-wall spectrum, are that unit operations costs are well established and it is also the only moderately-high-flux neutron irradiation source currently available for fusion-materials measurements.

The RFOM is given by

$$\text{RFOM} = \frac{AC(\text{M\$/yr})}{10 I_w(\text{MW/m}^2)V_{exp}(\text{m}^3)} \frac{1}{20} \qquad (18)$$

with AC = the annual charge, which is the sum of the actual operating cost and 15% of the facility capital cost, I_w = the average neutron wall-loading power within a specific experimental volume, and V_{exp} = the available experimental volume at an average wall loading, I_w. This expression assumes the ratio of dpa to uncollided neutron flux is $\cong 10$ dpa/(MW/m^2).

Table VI. Facility Cost Estimate Summary (1989 $U.S. Millions)[a]

	125 mA	250 mA	500 mA[b]	1000 mA
Accelerator systems				
Injector	0.8	1.6	3.2	6.4
Radio-frequency-quadrupole				
Structure (tank, rods, vacuum, cooling, stand)	1.1	2.2	4.4	8.8
RF power (tetrodes, DCPS, windows, coax)	0.7	1.4	2.8	5.6
Funnel and matching	0.5	1.3	2.6	5.2
Drift-tube-linac				
Structure (tanks, drift tubes, quads, vacuum)	7.3	7.3	14.6	29.2
RF power (klystrons, DCPS, windows, coax)	11.0	17.0	34.0	68.0
High-energy beam transport				
Quadrupoles, dipoles, vacuum	3.7	3.7	4.4	8.8
Non-linear optics	0.6	0.6	0.6	1.2
Energy-dispersion cavity	1.6	1.6	1.6	3.2
Tuneup beam stop	0.4	0.5	0.7	1.0
Beam splitter	1.7	1.7	0.0	0.0
Beam diagnostics				
Injector	0.2	0.4	0.8	1.6
DTL	0.4	0.4	0.8	1.6
HEBT	1.0	1.1	1.2	2.4
Controls system (15% of accelerator equipment)	4.7	6.1	10.8	21.5
Accelerator utilities				
Electric substation	1.2	1.8	3.5	6.5
Water cooling	1.2	1.8	3.5	6.5
Subtotal accelerator	38.1	50.5	89.5	177.5
Accelerator ED&I	6.0	9.0	12.0	15.0
Lithium target system				
Lithium jet and circulation system	3.0	4.5	9.0	18.0
Controls for lithium system	0.5	0.7	1.4	2.7
Test cell[c]				
Equipment	3.5	6.5	9.1	13.0
Controls for test cell	0.5	1.0	1.4	2.0
Balance of plant (buildings, utilities, shielding)[c]	55.0	78.0	110.0	156.0
Facility total (without contingency)	106.6	150.2	232.4	384.2

[a]Assumptions: (1) two lithium targets in all cases, (2) 125 mA: 1 RFQ, 1 DTL, HEBT beam splitting, (3) 250 mA: 2 RFQs, 1 DTL, HEBT beam splitting, (4) 500 mA: 4 RFQs, 2 DTLs, and (5) 1000 mA: 8 RFQs, 4 DTLs.
[b]Reference concept.
[c]Scaled from FMIT cost data.

Table VII. Annual Operating Costs (1989 $U.S. Millions)

|	125mA	250mA	500mA	1000mA	Unit
RF power	7.7	12.7	25.4	50.8	MW
AC power for RF ($e = 0.46$)	16.8	27.6	55.2	110.4	MW
Additional AC power (@ 20%)	3.4	5.5	11.0	22.0	MW
Total AC power	20.2	33.1	66.2	132.4	MW
Electric power costs ($0.035/kWh) (7500 hours/year-85%)	5.3	8.7	17.4	34.8	M$/y
Manpower	45.0	53.0	63.0	75.0	FTE
Manpower costs ($125K/FTE)	5.6	6.6	7.9	9.4	M$/y
Materials and services	2.0	3.0	4.5	6.8	M$/y
Target service costs	1.0	1.5	2.3	3.5	M$/y
Total operating costs	13.9	19.8	32.7	54.5	M$/y
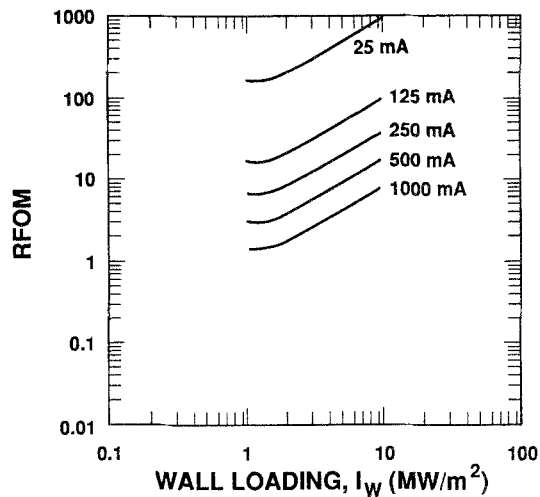
Fig. 35. Relative-figure-of-merit (FFTF = 1.0) for the D-Lithium source as a function of neutron wall loading, at various beam currents.

Lithium neutron source (in dollars per unit of damage) to the existing costs and capability of the FFTF. However, such a comparison ignores the qualitative advantage of making measurements with a source that simulates a fusion-reactor environment fairly closely, as opposed to the fast-fission neutron environment available at FFTF. The RFOM numbers derived using Eq. (18) should be divided by an assessment factor that accounts for the relative quality and usefulness of measurements that can be made at the D-Lithium and baseline facilities. Also, the RFOM does not reflect the extrapolations in physics and technology that may be needed to achieve the indicated performance from a given kind of neutron source.

7. CONCLUSIONS AND ASSESSMENTS

We have described a D-Lithium neutron source that would have five times the total deuteron current of FMIT, delivered to two targets positioned in an orthogonal configuration. For this reference system, the useful materials-test volume at a specific average uncollided neutron flux scales approximately as $[I_d]^{1.9}$, where I_d is the total deuteron current. The test volume available in the reference concept would therefore be 20 times greater than in FMIT (for the same average neutron flux). Beam-dynamics simulations show that a compact, high-frequency RFQ/DTL accelerator design is feasible at 250 mA, and that it should perform with small emittance growth and very low levels of beam loss. Target heating simulations show that the energy-deposition problem is tractable at 250 mA per target, with suitable manipulation of the beam energy spread and spatial profile in the HEBT.

From the volume/flux/current characteristics of the D-Lithium source given in Figs. 14 and 15, Eqs. (10) and (11), and the cost data of Tables VI and VII, the beam-current dependencies of cost, test volume at specific wall loading, and the RFOM are determined, and are summarized in Table VIII. For a 1000-mA deuteron current, where very large test volumes (400 liters) could be provided at moderate neutron wall-loading levels (1 MW/m²), the RFOM approaches that of the FFTF, but for high flux levels and reduced volumes the D-Lithium-source RFOM and cost per displacement is higher. The D-Lithium source RFOM is plotted in Fig. 35 as a function of neutron wall loading for various beam currents.

The RFOM provides a crude yardstick for comparing projected materials-testing costs of a D-

Table VIII. Dependence of Cost, Experimental Volume at Specific Neutron Flux, and Relative-Figure-of-Merit on D⁺ Beam Current

Beam current (mA)	125	250	500	1000
Operating cost (M$/yr)	13.9	19.8	32.7	54.5
Capital cost (M$)	106.7	150.2	232.4	384.2
Annual charge (M$/yr)[a]	29.9	42.3	67.6	112.1
I_w (MW/m²)[b]	Test volume (liters) (RFOM)			
1.0	8.8 (17.1)	31.0 (6.8)	110.0 (3.1)	390.0 (1.4)
2.0	3.6 (20.9)	12.7 (8.3)	45.0 (3.8)	159.6 (1.8)
5.0	0.6 (47.0)	2.3 (18.7)	8.0 (8.5)	28.4 (3.9)
10.0	0.2 (93.9)	0.6 (37.5)	2.0 (16.9)	7.1 (7.9)

[a]Operating cost + 15% of capital cost.
[b]Averaged over volume.

In a multi-module facility, each accelerator unit would be housed in a separately shielded vault so that maintenance could be carried out on any unit without shutting down the entire neutron output. This feature would increase overall facility availability for users.

The issues of radiation damage and activation of accelerator and target components have not been specifically addressed in this paper, but some general observations can be made. The maximum damage rate in either of the target back walls will be at the peak of (and proportional to) the beam current distribution and will be mainly that generated by the neutron flux from the adjacent lithium target. The damage contribution generated by neutrons from the orthogonal target will be less by a factor of 5–10 even at the most vulnerable location. Since the maximum value of the current density for the reference concepts is only 1/2 that in FMIT, we anticipate that target back-wall damage rates would actually be less than those estimated for FMIT, with correspondingly longer times between replacement.

Activation of the accelerator from beam loss due to halo formation is a design issue also not specifically addressed in this paper. The FMIT design anticipated that beam losses could be kept below a limit of 3 μA/m (3×10^{-5}/m), which would have permitted a mostly hands-on maintenance operation, with remote handling in some areas. With modern linac design techniques for improved control of beam emittance growth (listed in Section 2), and with the use of shielded emittance filters (beam scraping) if required, it should be possible to achieve lower beam-loss levels in the reference-system accelerator than specified for FMIT, even though the beam currents are higher by a factor of 2.5.

The modular accelerator approach suggested in this paper lends itself convincingly to various possible facility-staging scenarios. One can imagine a staging sequence that begins with a single linac module having an output current as low as 25 mA (1 RFQ), but which is designed with the correct choice of frequency, gradient, etc. to operate at up to 250 mA. The facility could be upgraded in steps by adding rf power, then a second RFQ, and then a second accelerator module to reach 500 mA. The final upgrade to 1000 mA would involve the addition of two more accelerator modules.

The construction cost of the reference D-Lithium concept would be similar to that estimated for FMIT (in escalated dollars), but would provide an order-of-magnitude greater materials-testing capability.

Projected operating costs and amortized construction costs show that in a 1000-mA D-Lithium facility, the relative cost per unit of materials damage produced would be similar to that at the FFTF. However, experimenters would have a much more appropriate neutron spectrum for simulating a fusion-reactor environment.

ACKNOWLEDGMENTS

REFERENCES

1. Materials for Fusion, A Report to the Fusion Power Coordinating Committee of the International Energy Agency by the Senior Advisory Panel (S. Amelinckx, Chairman), December 1986.
2. International Fusion-Materials-Irradiation-Facility (IFMIF) Workshop for the International Energy Agency, San Diego, California, February 14–17, 1989.
3. G. P. Lawrence, T. P. Wangler, S. O. Schriber, E. L. Kemp, M. T. Wilson, T. S. Bhatia, G. H. Neuschaefer, F. W. Guy, and D. D. Armstrong (1989). A high performance D-lithium neutron source for fusion technology testing: Accelerator driver design. *Fusion Tech.*, 15(2), 289.
4. F. M. Mann (1989). IFMIF, An accelerator-based neutron source for fusion components irradiation testing. *Fusion Tech.*, 15(2), 295.
5. G. P. Lawrence, T. S. Bhatia, B. Blind, F. W. Guy, R. A. Krakowski, G. H. Neuschaefer, N. M. Schnurr, S. O. Schriber, G. L. Varsamis, T. P. Wangler, and M. T. Wilson, High-Performance Deuterium-Lithium Neutron Source for Fusion Materials and Technology Testing, Proc. 1989 Particle Accelerator Conf., Chicago, Illinois, March 20–23, 1989 (to be published).
6. A. L. Trego, J. W. Hagan, E. K. Opperman, and R. J. Burke (1983). Fusion materials irradiation test facility—A facility for fusion materials qualification (Part 2). *Nucl. Tech. Fusion*, 4(2), 695.
7. G. H. Gillespie, Y. Y. Kuo, D. Keefe, and T. P. Wangler, eds., High-Current, High-Brightness and High-Duty Factor Ion Injectors, La Jolla Institute, 1985, AIP Conf. Proc., 1986, p. 139.
8. T. P. Wangler, Physics Design of Linear Accelerators for Intense Ion Beams, Proc. 1988 Linear Accelerator Conf., Williamsburg, Virginia, October 1988 (to be published).
9. R. Serber (1947). The production of high energy neutrons by stripping. *Phys. Rev.*, 72(11), 1008–1016.
10. M. R. Shubaly (1979). High current DC ion source development at CRNL. *IEEE Trans. Nucl. Sci.*, NS-26(3), 3065.

11. A. J. Jason, B. Blind, and E. M. Svaton, Uniform Ribbon-Beam Generation for Accelerator Production of Tritium, Proc. 1988 Linear Accelerator Conf., Williamsburg, Virginia, October 1988 (to be published).

12. F. M. Mann, F. Schmittroth, and L. L. Carter, Neutrons from D + Li and the FMIT Irradiation Environment, Hanford Engineering Development Laboratory Report HEDL-TC-1459, November 1981.

13. H. A. Bethe (1933). Quantenmechanik der Ein- und Zwei-Elektronenprobleme. In *Handbuch der Physik* (Vol. 24, No. 1), H. Geiger and K. Scheel, eds. (Springer-Verlag, Berlin), p. 491.

14. U. Fano (1963). Penetration of protons, alpha particles, and mesons. *Annu. Rev. Nucl. Sci.*, **13**, 1–66.

15. J. F. Ziegler, J. P. Biersack, and U. Littmark (1985). *The Stopping and Range of Ions in Solids* (Vol. 1) (Pergamon Press, Oxford).

16. J. A. Hassberger, Preliminary Assessment of Interactions between the FMIT Deuteron Beam and Liquid Lithium Target, Hanford Engineering Development Laboratory Report, HEDL-TME 82-28, March 1983.

17. S. V. Patankar and D. B. Spalding (1970). *Heat and Mass Transfer in Boundary Layers, A General Calculation Procedure* (2nd Ed.) (Intertext Books, London).

18. D. Rockwell, S. Johnson, and J. C. Chen (1976). Thermo-Fluid Analysis of a Deuteron-Lithium Target, TS-761 (Department of Mechanical Engineering and Mechanics, Lehigh University, Bethlehem, Pennsylvania).

19. M. Abdou et al., Blanket Comparison and Selection Study, Interim Report, ANL/FPP/TM-177, Argonne National Laboratory, September, 1983.

20. C. B. Bathke, R. A. Krakowski, R. L. Miller, and K. A. Werley (1989). The reversed-field pinch (RFP) fusion-neutron source: A conceptual design. *J. Fusion Energy*, **8**(3).

21. R. A. Krakowski, J. D. Sethian, and R. L. Hagenson, The high-density Z-pinch as a pulsed fusion neutron source for fusion nuclear technology and materials testing. *J. Fusion Energy*, **8**(3).